Comparative Study of Some Population-Based Optimization Algorithms on Inverse Scattering of a Two-Dimensional Perfectly Conducting Cylinder in Dielectric Slab Medium

Chien-Ching Chiu, Chi-Hsien Sun, Ching-Lieh Li, and Chung-Hsin Huang

***Abstract*—The application of four techniques for the shape reconstruction of a 2-D metallic cylinder buried in dielectric slab medium by measured the scattered fields outside is studied in the paper. The finite-difference time-domain (FDTD) technique is employed for electromagnetic analyses for both the forward and inverse scattering problems, while the shape reconstruction problem is transformed into optimization one during the course of inverse scattering. Then, four techniques including asynchronous particle swarm optimization (APSO), PSO, dynamic differential evolution (DDE) and self-adaptive DDE (SADDE) are applied to reconstruct the location and shape of the 2-D metallic cylinder for comparative purposes. The statistical performances of these algorithms are compared. The results show that SADDE outperforms PSO, APSO and DDE in terms of the ability of exploring the optima. However, these results are considered to be indicative and do not generally apply to all optimization problems in electromagnetics.**

***Index Terms*—Asynchronous particle swarm optimization (APSO), cubic spline, dynamic differential evolution (DDE), finite difference time domain (FDTD), inverse scattering, particle swarm optimization (PSO), self-adaptive dynamic differential evolution (SADDE), time domain.**

I. Introduction

THE detection and reconstruction of buried and inaccessible scatterers by inverting microwave electromagnetic measurements is a research field of considerable interests because of its numerous applications in geophysical prospecting, through-wall imaging, and nondestructive testing [1]–[5]. The reconstruction of the location, shape, and/or size of metallic cylinders in a three-layer material medium may find its application for detection of water pipes inside the wall. Paper [6] emphasizes on the profile reconstruction of the second layer for the three-layer structure.

Numerical researches about inverse scattering found in the literature are based on either frequency-domain and/or time-domain approaches, or most of them belong to the former [7]–[9]. However, the time-domain scheme is a potential alternative for the inverse problems. For frequency-domain algorithms, the interaction of the entire medium with the incident field needs to be considered. In contrast, since the data of time-domain scattered field contain more information about the scatterer than those in the scattered data of single frequency, time-domain approaches can exploit causality to limit the region of inversion. Time-domain inverse scattering problems thus draw considerable interests in the area of remote sensing.

It is well known that one of the major difficulties for the inverse scattering is its ill-posedness in nature. The ill-posedness can be treated via the idea of regularization [10]. Another concern for inverse scattering is due to the nonlinearity because it involves the product of two unknowns: the electrical properties of object and the electric field within the object.

Inverse scattering problems are usually cast into optimization ones. There are usually two types of optimization schemes to solve the inverse scattering problems: the deterministic one and the stochastic one. The former has been developed for decades, such as the contrast source inversion method [11], conjugate-gradient method [12], distorted Born iterative method [13], the level set method [5], [14] and other gradient-type methods [15], [16]. Based on these deterministic techniques, several multi-resolution methods have been proposed to increase the efficiency of the inversion, such as those in [14], [17]–[19] and the references therein. The stochastic methods usually employ a group of initial guesses and use certain stochastic procedure to minimize the cost function (CF), such as the genetic algorithm (GA) [16], [20], [21] and various evolutionary optimization ones. The application of population-based optimization techniques increases the capability of finding the global minimum rather than being trapped in a local minimum as the deterministic optimization techniques are. Evolutionary computation [22], [23] provides a more robust and efficient approach for solving inverse scattering problems. Particle swarm optimization (PSO) has proven to be a useful method of optimization for difficult and discontinuous multidimensional engineering problems [24]–[26] due to its efficiency of exploring the entire search space. Moreover, PSO had been applied for inverse scattering problems [27]–[33]. Another method, called dynamic differential evolution (DDE) is able to provide the global optimization procedure as GA does, but in a new and faster way. In additions, DDE were utilized to search the global extreme of the inverse scattering problem to overcome the drawback of the deterministic methods [31], [33]–[37].

Manuscript received May 5, 2011; revised December 23, 2011 and March 20, 2012; accepted June 24, 2012. Date of publication August 27, 2012; date of current version March 21, 2013. This work was supported by National Science Council, Republic of China, under Grant NSC-100-2221-E-032-057- and NSC-100-2221-E-032-058-.

C.-C. Chiu, C.-H. Sun, and C.-L. Li are with the Department of Electrical Engineering, Tamkang University, New Taipei City 25137, Taiwan (e-mail: chiu@ee.tku.edu.tw; laisingsun@yahoo.com.tw; li@ee.tku.edu.tw).

C.-H. Huang is with the Department of Computer and Communication Engineering, Taipei College of Maritime Technology, New Taipei City 25137, Taiwan (e-mail: havehuang@hotmail.com).

Digital Object Identifier 10.1109/TGRS.2012.2208756

In [32], it was shown that PSO outperforms real-coded GA in terms of convergence speed. In recent decades, some papers have compared different algorithms applied for inverse scattering problems [30], [31], [33]. However, these methods are reported with certain drawbacks that are usually related to the intensive computational effort required to achieve the global optimum and/or the possibility of premature convergence to local optima. Hence, it is seemingly natural to use evolutionary algorithms (EAs), not only to find the solutions of a problem but also to tune these algorithms to the particular problem. Technically speaking, it is usually demanded to modify the value of control parameters for the algorithm during the search progress. The proof of convergence of EAs with self-adaptation is difficult because the control parameters are changed randomly and the selection does not affect their evolution directly [38]. Since DDE is a promising instance of EAs, for which it is interesting to investigate how self-adaptivity can be applied. Until now, self-adaptive DE (SADE) applied to the problems of real-valued antenna and microwave circuit design was reported [39], but no papers have ever applied SADDE to investigate the inverse scattering problems.

In this paper, four different evolutionary techniques for inverse scattering problems through time-domain approach are compared. The electromagnetic analysis is accomplished by using the finite-difference time-domain (FDTD) method, for which the sub-gridding technique [20], [37], [40] is implemented to closely describe the fine structure of the cylinder. The inverse problem is formulated into an optimization one, and then four techniques including asynchronous PSO (APSO, PSO, DDE, and SADDE are applied to search the parameter space. Cubic-spline interpolation technique [41] is employed to reduce the number of parameters needed to closely describe a cylinder of arbitrary shape as compared to the Fourier series expansion.

In Section II, the sub-gridding FDTD method for the electromagnetic analysis of the forward problem is described. In Section III, the differences of the four EAs are given. In Sections IV and V, the inverse problem and some numerical results are presented, respectively. Finally, in Section VI, some conclusions are drawn.

II. Forward Problem

Let us consider a two-dimensional (2-D) three-layer structure with a buried metallic cylinder in the second layer as shown in Fig. 1. The metallic cylinder is parallel to z-axis and is buried between the planar interfaces separating three homogeneous spaces: region 1 (ε_1, μ_1), region 2 (ε_2, μ_2), and region 3 (ε_3, μ_3). The metallic cylinder is illuminated by a line source with Gaussian pulse shape placed at two different positions sequentially denoted by Tx in the first layer, and then the scattered E fields are recorded simultaneously at those points denoted by Rx in the same layer. The shape of cross section of the object is star-like that can be represented in polar coordinates with respect to the origin (X_O, Y_O) of the local coordinate in x-y plane as shown in Fig. 2.

The electromagnetic analysis is accomplished by using the FDTD method, for which the computational domain is discretized by using Yee cells [42]. It should be mentioned that the computational domain is surrounded by pre-optimized perfect matching layers [43] to reduce the reflection from the domain boundary. The direct scattering problem is to calculate the scattered electric fields while the shape and location of the scatterer is given. The shape function $F(\theta)$ of the scatterer is described by the trigonometric series in the direct scattering problem as follows:

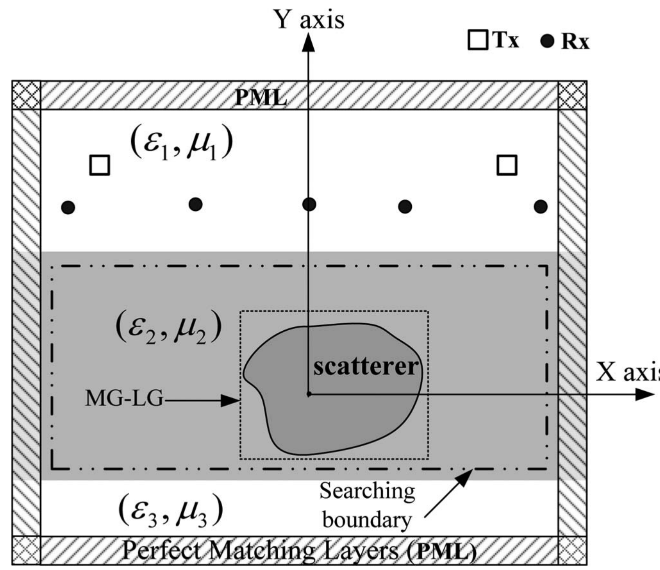

Fig. 1. Geometry for the inverse scattering of a metallic cylinder of arbitrary shape in slab medium.

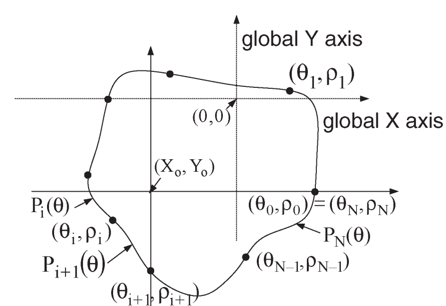

Fig. 2. Cylinder of arbitrary shape is described in terms of a closed cubic spline. The cubic spline consists of the polynomials of degree 3. (X_O, Y_O) is the center position in the x-y plane. The $\rho_1, \rho_2, \ldots, \rho_N$ are radius parameters to describe cylinder.

$$F(\theta) = \sum_{n=0}^{\frac{N}{2}} B_n \cos(n\theta) + \sum_{n=1}^{\frac{N}{2}} C_n \sin(n\theta) \tag{1}$$

where Bn and Cn are real coefficients to expand the shape function.

In order to closely describe the shape of the cylinder for both the forward and inverse scattering procedure, the sub-gridding technique is implemented in the FDTD code; the details are presented in [40].

III. EAs

Evolution algorithm starts with an initial population of potential solutions that is composed by a group of randomly generated individuals which represents the center position and the geometrical radii of the cylinder. Each individual is a D-dimensional vector consisting of D optimization parameters.

The initial population may be expressed by $\{X_j : j = 1, 2, \ldots, Np\}$, where Np is the population size. The explicit expression for X_j is given in next section. The details of the DDE, SADDE, PSO, and APSO algorithms are given below.

A. DDE

In DDE, after generating the initial population, the candidate solutions are refined by applying mutation, crossover, and selection, iteratively. The flowchart of the DDE algorithm is shown in Fig. 3. In this strategy, a mutant vector for each target vector V_j^{k+1} at the $k+1$ generation is computed by

$$\begin{aligned}\left(V_j^{k+1}\right) i = \left(X_j^k\right) i + \zeta \cdot \left[\left(X_{\text{best}}^k\right) i - \left(X_j^k\right) i\right] \\ + \chi \cdot \left[\left(X_m^k\right) i - \left(X_n^k\right) i\right], \\ j, m, n \in [0, N_p - 1], \qquad m \neq n \end{aligned} \tag{2}$$

where $i = 1 \sim D$ and χ and ζ are the scaling factors associated with the vector differences $(X_{\text{best}}^k - X_j^k)$ and $(X_m^k - X_n^k)$, respectively. The disturbance vector V due to the mutation mechanism consists of parameter vector X_j^k, the best particle X_{best}^k and two randomly selected vectors. As comparison, the mutant vector V_j^{k+1} is generated according to (3) for typical DE [44]

$$\begin{aligned}\left(V_j^{k+1}\right) i = \left(X_j^k\right) i + \chi \cdot \left[\left(X_m^k\right) i - \left(X_n^k\right) i\right], \\ j, m, n \in [0, N_p - 1], \quad m \neq n \end{aligned} \tag{3}$$

where $i = 1 \sim D$ and χ is the scaling factor associated with the vector difference $(X_m^k - X_n^k)$. Note that ζ is set to zero for DE; therefore, the main differences between DDE and DE is that DDE includes the idea of approaching the "Best" during the course of optimization procedure.

After mutation, the crossover operator is applied to generate another kind of new vector u_j. The crossover operation in DDE delivers the crossover vector u_j^{k+1} by mixing the components of the current vector X_i and the above mutant vector V_i. It can be expressed as

$$u_j^{k+1} = \begin{cases} \left(V_j^{k+1}\right)_i, & Q_k < CR \\ \left(X_j^k\right)_i, & Q_k \geq CR \end{cases} \tag{4}$$

where $i = 1 \sim D$ and Q_k is a random number uniformly distributed within [0,1]. $CR \in (0, 1)$ is a predefined crossover rate. DDE uses a greedy selection operator that is defined by

$$X_j^{k+1} = \begin{cases} u_j^{k+1}, & \text{if} \quad \mathrm{CF}\left(u_j^k\right) < \mathrm{CF}\left(X_j^k\right) \\ X_j^k, & \text{otherwise.} \end{cases} \tag{5}$$

Selection operation is conducted by comparing the parent vector X_j^{k+1} with the crossover vector u_j^{k+1}. The vector with smaller CF value is selected as a member for the next generation.

B. SADDE

Storn has suggested [44] to choose the DE control parameters χ and CR from the intervals [0.5,1] and [0.8,1], respectively, and to set $Np = 10D$. However, the suitable parameter value

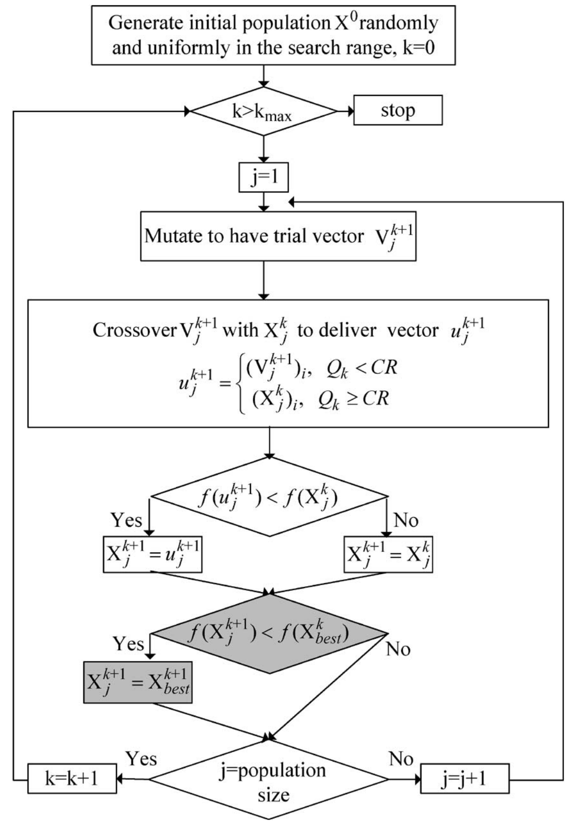

Fig. 3. Flowchart for the dynamic differential evolution. Pessimistic sub-area stands for dynamic update.

is, frequently, problem dependent. The control parameters that work fine for one problem may fail to lead to convergence for other problems. The effort of trial-and-error to fine tune the control parameter is unavoidable usually. In some cases, the effort and time for this trial-and-error is unacceptable. In [38], [39] a novel strategy is proposed for the self-adapting of control parameters for DE. The basic idea is to have the control parameters evolve through generations. New vectors are generated by using the evolved values of the control parameters. These new vectors are more likely to survive and produce offspring during the selection procedure. In turn, the survived vectors carry the improved values of the control parameters to the next generation. Therefore, the control parameters are self-adjusted in every generation for each individual according to the following scheme:

$$\zeta_{i,k+1} = \begin{cases} \zeta_l + rand_1 * \zeta_u, & \text{if } rand_2 < 0.1 \\ \zeta_{i,k}, & \text{otherwise} \end{cases} \tag{6}$$

$$\chi_{i,k+1} = \begin{cases} \chi_l + rand_3 * \chi_u, & \text{if } rand_4 < 0.1 \\ \chi_{i,k}, & \text{otherwise} \end{cases} \tag{7}$$

$$CR_{i,k+1} = \begin{cases} rand_5, & \text{if } rand_6 < 0.1 \\ CR_{i,k}, & \text{otherwise} \end{cases} \tag{8}$$

where $rand1$, $rand2$, $rand3$, $rand4$, $rand5$, and $rand6$ are random numbers with the values uniformly distributed between 0 and 1. ζ_l, ζ_u, χ_l, and χ_u are the lower and the upper limits of ζ and χ, respectively. Both ζ_l and χ_l are set to 0.1, and both ζ_u and χ_u are set to 0.9 [38], [39]. The performance of SADE applied to several low-dimensional benchmark functions is reported. It is concluded that the self-adaptive strategy is better (or at least comparable) to the classical DE strategy regarding the quality of the solutions obtained. The algorithm of SADDE is a self-adaptive version of DDE, which is processed of self-adaptibility and the ability of approaching the "Best." Based on the self-adaptive concept, the parameters ζ, χ, and CR adjust automatically while the time complexity does not increase.

C. PSO

In PSO, the particles move in the search space, where each particle position is updated by two optimum positions. The first one is the position (with best fitness) that has been achieved so far for the concerned particle. This position is called x_{pbest}. The other one is the global best position obtained so far by any particle in the swarm. This best position is called x_{gbest} [45].

By keeing x_{pbest} and x_{gbest}, the update rule for the velocity of each particle is an important mechanism in a PSO algorithm. The most commonly used update rule for the velocity v_j^{k+1} is as follows:

$$v_j^{k+1} = \omega \cdot v_j^k + c_1 \cdot \phi_1 \cdot \left(x_{pbest_j}^k - x_j^k\right) + c_2 \cdot \phi_2 \cdot \left(x_{gbest}^k - x_j^k\right) \tag{9}$$

$$x_j^{k+1} = x_j^k + v_j^{k+1}, \quad j = 0 \sim N_p - 1 \tag{10}$$

where c_1 and c_2 are the learning coefficients used to control the impact of the local and global components in velocity (9). v_j^{k+1} and x_j^{k+1} are the velocity and position of the jth particle at generation $k+1$. Both ϕ_1 and ϕ_2 are random numbers with the values uniformly distributed between 0 and 1. ω is a parameter known as the inertia weight.

D. APSO

Clerc [46] suggested the use of a different velocity update rule, which introduced a parameter ξ called constriction factor. The role of the constriction factor is to ensure convergence when all the particles tend to stop their movement. The flowchart of the APSO algorithm is shown in Fig. 4.

The velocity update rule is then given by

$$v_j^{k+1} = \xi \cdot \left(v_j^k + c_1 \cdot \phi_1 \cdot \left(x_{pbest_j}^k - x_j^k\right) + c_2 \cdot \phi_2 \cdot \left(x_{gbest}^k - x_j^k\right)\right) \tag{11}$$

$$x_j^{k+1} = x_j^k + v_j^{k+1}, \quad j = 0 \sim N_p - 1 \tag{12}$$

where $\xi = 2/|2 - \phi - \sqrt{\phi^2 - 4\phi}|$, $\phi = c_1 + c_2 \geq 4$.

By (9) and (11), particles fly around in the multidimensional solution space and adjust their positions according to their own experience and the experience of neighboring particles, by exploiting the knowledge of best positions encountered by themselves and their neighbors [32].

The key distinction between a PSO and the APSO is on the updating mechanism, damping boundary condition, and mutation scheme. In the typical synchronous PSO, the algorithm updates all the particles velocities and positions using (9) and (11) at the end of each generation and then updates the best positions, x_{pbest} and x_{gbest}. Alternatively, the current updating mechanism of APSO uses the following rule: just after the

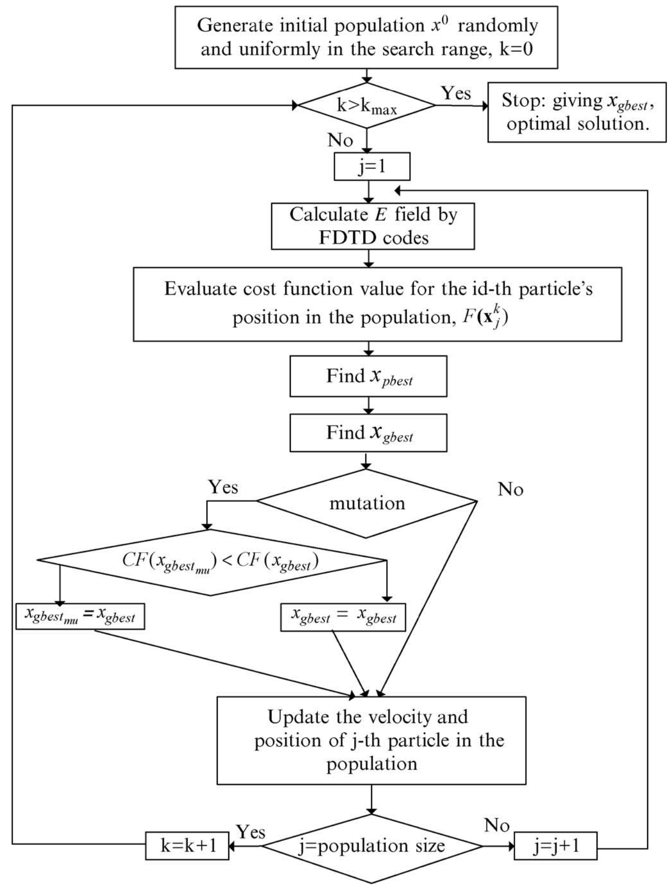

Fig. 4. Flowchart for the APSO.

update by (9) and (11) for each particle the best positions x_{pbest} and x_{gbest} will be replaced if the new position is better than the current best ones such that they can be used immediately for the next particle. In this way, the swarm reacts more quickly to speedup the convergence.

Boundary conditions in PSO play a key role as it is pointed out in [47]. In this paper, we have applied the damping boundary condition and mutation scheme. The mutation scheme plays a role in avoiding premature convergences for the searching procedure and helps the x_{gbest} escape from the local optimal position. More details about the APSO algorithm can be found in [29], [30].

IV. Inverse Problem

A. Cubic-Spline Representation for the Cross-Section Shape of Scatterer

There are two main advantages for cubic-spline expansion as following: 1) for complicated shape, the number of unknowns for expanding the shape function by cubic-spline expansion is less than that by Fourier series expansion, 2) the exact center of the object is insensitive for cubic-spline expansion unlike for Fourier series expansion. If there is some displacement for the exact center of the object, the number of unknowns for expanding the shape function by Fourier series expansion will increase largely. On the other hand, the number of unknowns does not vary for cubic-spline expansion [48].

It should be noted that for the inverse problem, the shape function of the 2-D metallic cylinder is described by a cubic spline in this study instead of the trigonometric series described in the section of the forward problem. The cubic spline is more efficient in terms of the unknown number required to describe a cylinder of arbitrary cross section. By using the cubic spline, the coordinates of local origin inside the cylinder serve as the searching parameter and can move around the searching space, which is difficult (if not impossible) if the trigonometric series expansion is used in the inversion procedure.

As shown in Fig. 2, the cubic spline consists of connected curve segments described by the polynomials of degree 3 $P_i(\theta)$, $i = 1, 2, \ldots, N$. The connected segments satisfy the following continuous conditions:

$$\begin{aligned} &P_i(\theta_i) = P_{i+1}(\theta_i) \equiv \rho_i \\ &P_i'(\theta_i) = P_{i+1}'(\theta_i) \qquad\qquad i = 1, 2, \ldots, N \\ &P_i''(\theta_i) = P_{i+1}''(\theta_i) \end{aligned} \tag{13}$$

$$\begin{aligned} &P_1(\theta_0) = P_N(\theta_N) \\ &P_1'(\theta_0) = P_N'(\theta_N) \equiv \rho_N' \\ &P_1''(\theta_0) = P_N''(\theta_N). \end{aligned} \tag{14}$$

Through the interpolation of the cubic spline, an arbitrary smooth cylinder can be easily described through the radius parameters $\rho_1, \rho_2, \ldots, \rho_N$ and the slope ρ_N'. As long as $\rho_1, \rho_2, \ldots, \rho_N$ and ρ_N' are given, the continuous conditions can yield a system of algebraic equations to determine all the polynomials of degree 3, of which the details are referred to [41]. By combining the four optimization algorithms and the cubic-spline interpolation technique, we are able to reconstruct the microwave image efficiently.

B. Inverse Problem

For the inverse scattering problem, the shape and location of the perfectly conducting cylinder are reconstructed by the given scattered electric field recorded at the receivers. The inverse problem is resolved by an optimization approach, and four techniques including DDE, SADDE, PSO, and APSO are applied to minimize the following CF (CF):

$$CF = \frac{\sum_{n=1}^{N_i} \sum_{m=1}^{M} \sum_{b=0}^{B} \left| E_z^{exp}(n, m, b\Delta t) - E_z^{cal}(n, m, b\Delta t) \right|}{\sum_{n=1}^{N_i} \sum_{m=1}^{M} \sum_{b=0}^{B} \left| E_z^{exp}(n, m, b\Delta t) \right|} \tag{15}$$

where E_z^{exp} and E_z^{cal} are the recorded electric field data and the calculated electric fields, respectively. N_i and M are the total number of the transmitters and receivers, respectively. B is the total number of time step to record the electric fields.

It should be noted that the coordinates of local origin inside the cylinder plus the radii of the geometrical spline used to describe the shape of the cylinder will be determined by DDE, SADDE, PSO, and APSO schemes. In other words, the D-dimensional vector X_j that forms the parameter space can expressed more explicitly as: $X_j = \{X_{j,i}; i = 1, 2, \ldots, D\}$, where $X_{j,1} = X_O$, $X_{j,2} = Y_O$, $X_{j,i} = \rho_i$, $i = 3, \ldots\ldots, D - 1$, $X_{j,D} = \rho_N'$. The termination criterion is set to 1000 generations in our simulation.

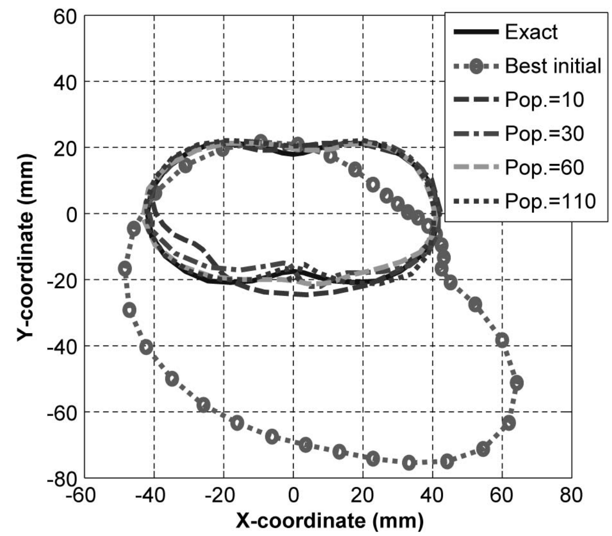

Fig. 5. Exact, reconstructed by SADDE with different population size, and best initial solution. The shape function of this object is given by $F(\theta) = 29.75 + 11.9\cos(2\theta)$ mm.

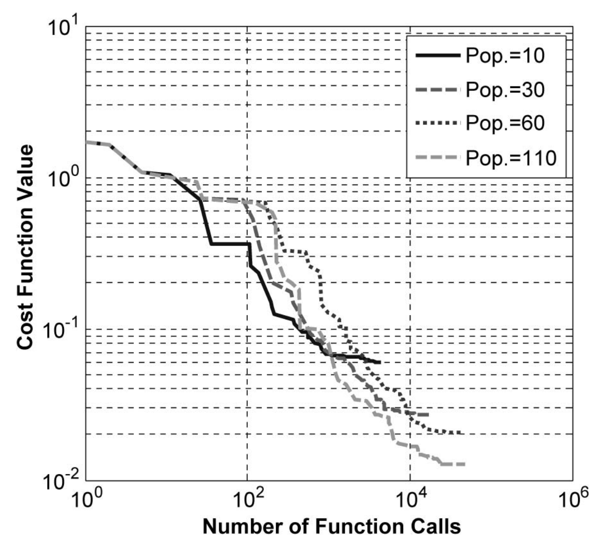

Fig. 6. Cost function (CF) versus numbers of function calls for example 1 by SADDE. The shape function of this object is given by $F(\theta) = 29.75 + 11.9\cos(2\theta)$ mm.

V. Numerical Results

In this paper, we compare SADDE with PSO, APSO, and DDE algorithms. The control parameters for the last three algorithms are those that commonly adopted by other research works, and good performances are reported. We apply these algorithms to microwave imaging to investigate the effects of single and multiple objects, synthetic object and non-synthetic object, and also the locations of the transmitters.

For Fig. 1, the problem space is divided in 68 × 68 grids with the grid size $\Delta x = \Delta y = 5.95$ mm. The metallic cylinder is buried in lossless slab medium $(\sigma_1 = \sigma_2 = \sigma_3 = 0)$. The transmitters and receivers are placed in free space above the homogeneous dielectric slab. The permittivities in region 1, region 2, and region 3 are characterized by $\varepsilon_1 = \varepsilon_0$, $\varepsilon_2 = 8\varepsilon_0$, and $\varepsilon_3 = \varepsilon_0$, respectively, while the permeability μ_0 is assumed for each region, i.e. only non-magnetic media are concerned here.

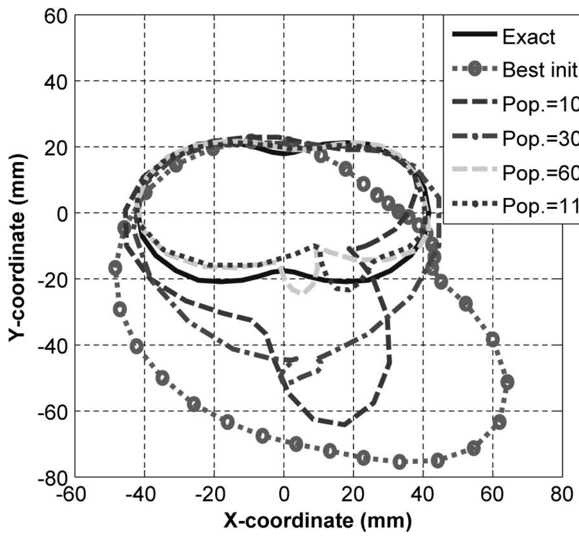

Fig. 7. Exact, reconstructed by DDE with different population size, and best initial solution. The shape function of this object is given by $F(\theta) = 29.75 + 11.9\cos(2\theta)$ mm.

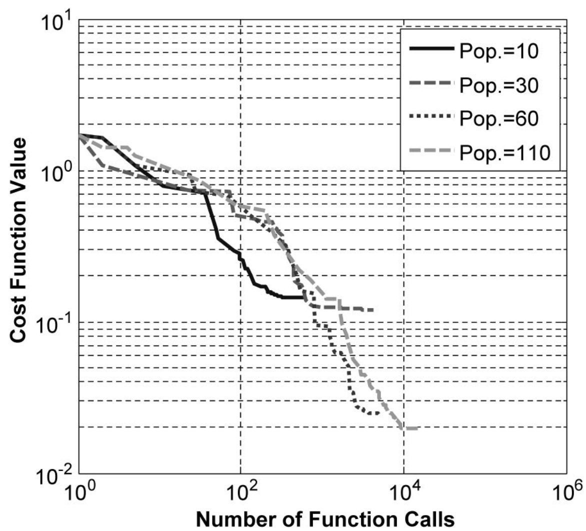

Fig. 8. Cost function (CF) versus numbers of function calls for example 1 by DDE. The shape function of this object is given by $F(\theta) = 29.75 + 11.9\cos(2\theta)$ mm.

The cylindrical object is illuminated by a transmitter at two different positions, $N_i = 2$, which are located at the $(-143$ mm, 178.5 mm) and (143 mm, 178.5 mm), respectively. The scattered E fields for each illumination are collected at five receivers, $M = 5$, which are equally separated by 47.8 mm along the line at a distance of 48 mm from the interface between region 1 and region 2. The excitation waveform $I_z(t)$ of the transmitter is the Gaussian pulse, given by

$$I_z(t) = \begin{cases} Ae^{-\alpha(t-\beta\Delta t)^2}, & t \le T_w \\ 0, & t > T_w \end{cases} \tag{16}$$

where $A = 1000$, $\beta = 24$, $\Delta t = 13.337$ ps, $\alpha = (1/4\beta\Delta t)^2$, and $T_w = 2\beta\Delta t$. The time duration is set to 250 Δt. Note that in order to accurately describe the shape of the cylinder, the subgridding FDTD technique is used both in the forward scattering $(1:9)$ and the inverse scattering $(1:5)$ parts—but with different scaling ratios as indicated in the parentheses.

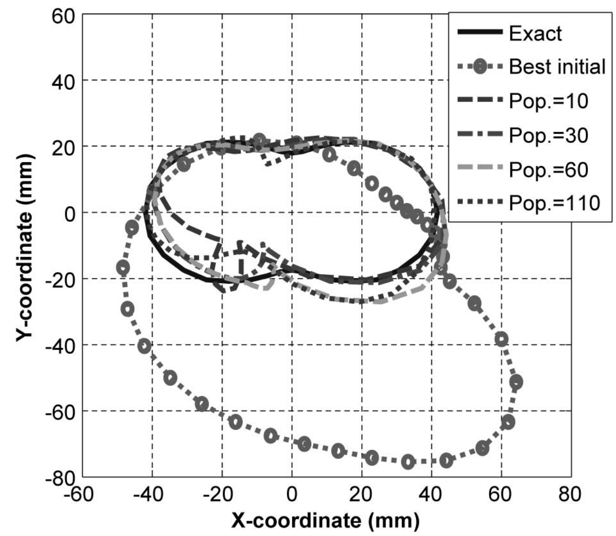

Fig. 9. Exact, reconstructed by APSO with different population size, and best initial solution. The shape function of this object is given by $F(\theta) = 29.75 + 11.9\cos(2\theta)$ mm.

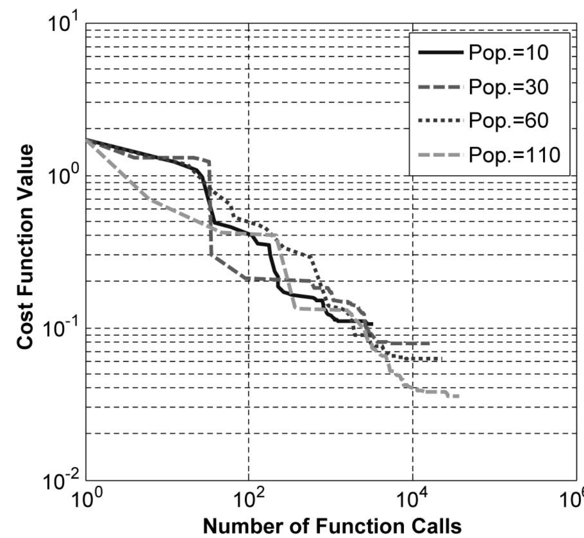

Fig. 10. Cost function (CF) versus numbers of function calls for example 1 by APSO. The shape function of this object is given by $F(\theta) = 29.75 + 11.9\cos(2\theta)$ mm.

The following examples are investigated for the inverse scattering of the proposed structure by using SADDE, DDE, APSO, and PSO, respectively. There are 11 unknown parameters to retrieve, which include the center position (X_O, Y_O), the radius ρ_i, $i = 1, 2, \ldots, 8$, of the shape function and the slope ρ'_N. Very wide searching ranges are used for these four optimization techniques to optimize the CF given by (15). The parameters and the corresponding searching ranges are listed follows: -47.6 mm $\le X_O \le 47.6$ mm, -47.6 mm $\le Y_O \le 47.6$ mm, 5.95 mm $\le \rho_i \le 71.4$ mm, $i = 1, 2, \ldots, 8$, $-2 \le \rho'_N \le 2$. The crossover rate CR is set to be 0.8. Both parameters ζ and χ are set to be 0.8 in DDE. In our simulation, DDE and SADDE use the same stopping criteria. The related coefficients of the APSO are set below. The learning coefficients c_1 and c_2 are set to 2.8 and 1.3, respectively, [49]. The mutation probability is 0.4.

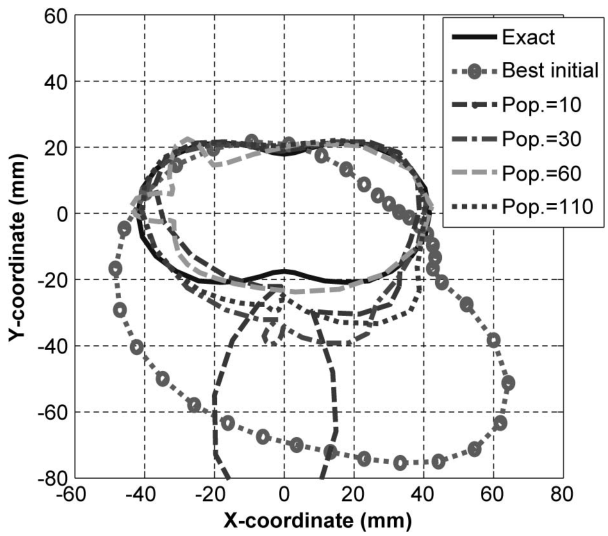

Fig. 11. Exact, reconstructed by PSO with different population size, and best initial solution. The shape function of this object is given by $F(\theta) = 29.75 + 11.9\cos(2\theta)$ mm.

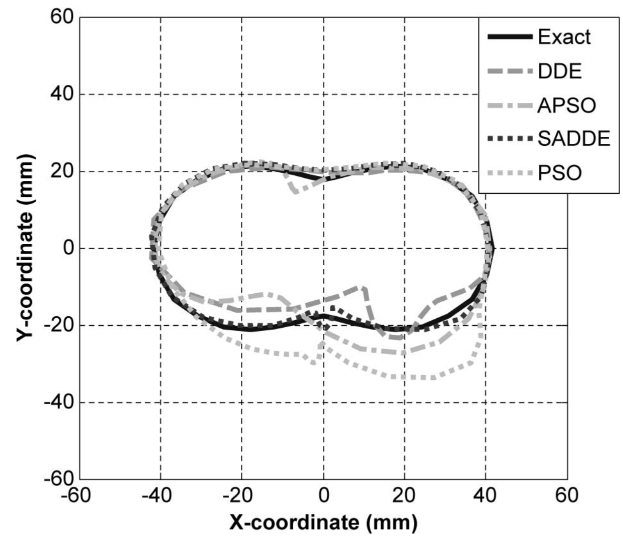

Fig. 13. Reconstructed cross section of the cylinder of example 1 by DDE, APSO, SADDE, and PSO. The shape function of this object is given by $F(\theta) = 29.75 + 11.9\cos(2\theta)$ mm.

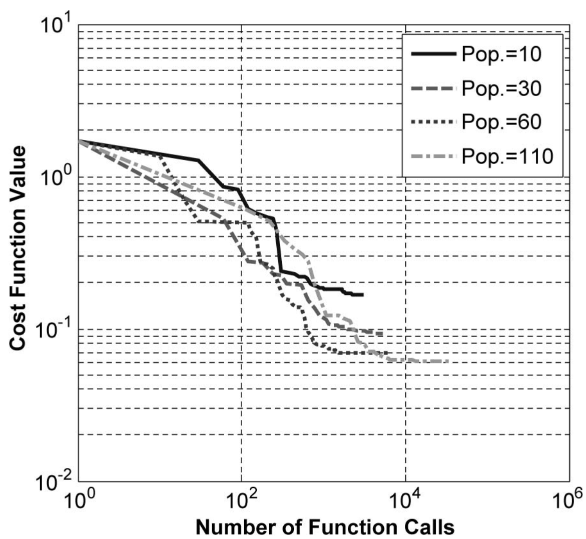

Fig. 12. Cost function (CF) versus numbers of function calls for example 1 by PSO. The shape function of this object is given by $F(\theta) = 29.75 + 11.9\cos(2\theta)$ mm.

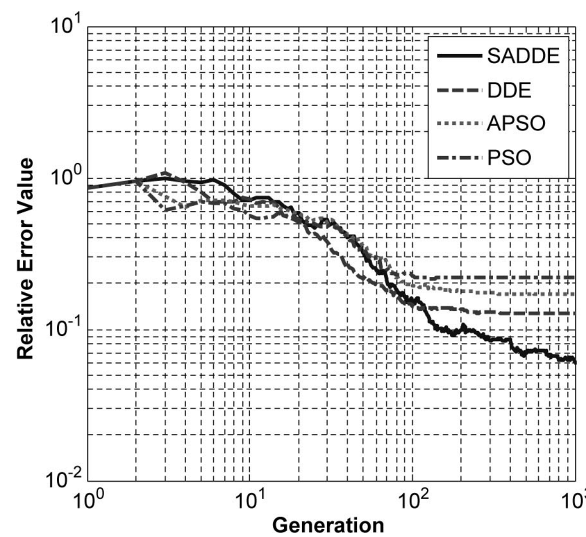

Fig. 14. Shape function error versus generation for example 1 by SADDE, DDE, APSO, and PSO, respectively. The shape function of this object is given by $F(\theta) = 29.75 + 11.9\cos(2\theta)$ mm.

Here, relative error for the shape reconstruction is defined as

$$\text{Relative Error} = \left\{ \frac{1}{N'} \sum_{i=1}^{N'} \left[F^{cal}(\theta_i) - F(\theta_i) \right]^2 / F^2(\theta_i) \right\}^{1/2} \tag{17}$$

where the N' is set to 720.

Reconstruction is carried out on an Intel PC (2.83 GHz/ 2G memory/500 G). The software is developed on FORTRAN VISION 6.0 in WINDOWS XP system environment.

A. Variation of the Population Size

At first, two reconstruction cases are tested. For the first example, the metallic cylinder with shape function $F(\theta) = 29.75 + 11.9\cos(2\theta)$ mm is considered. Four different population sizes, i.e., Pop $= 10$, 30, 60, and 110 have been examined for SADDE, DDE, APSO, and PSO, while the total number of iterations is set equal to 1000. Furthermore, 20 runs for each population size are executed for SADDE, DDE, APSO, and PSO, respectively. It is mentioned that the initial population is identical for the same run by SADDE, DDE, APSO, and PSO, respectively.

Fig. 5 shows the exact metallic cylinder, and the reconstructed results derived by SADDE after 1000 iterations for Pop. $= 10$, 30, 60, and 110, respectively. The convergence rate of the average CF after 20 runs for this example is given in Fig. 6. Moreover, the numerical results about the reconstruction and convergence rate of the average CF (after 20 runs) by the other three algorithms DDE, APSO, and PSO are shown in Figs. 7–12, respectively. It is obvious that when the population size is increased the reconstruction quality is improved for all algorithms. The final reconstructed shapes delivered by the four algorithms at the 1000th generation are plotted in Fig. 13 as compared to the exact one. The relative error of the reconstructed shape $F^{cal}(\theta)$ with respect to the exact one

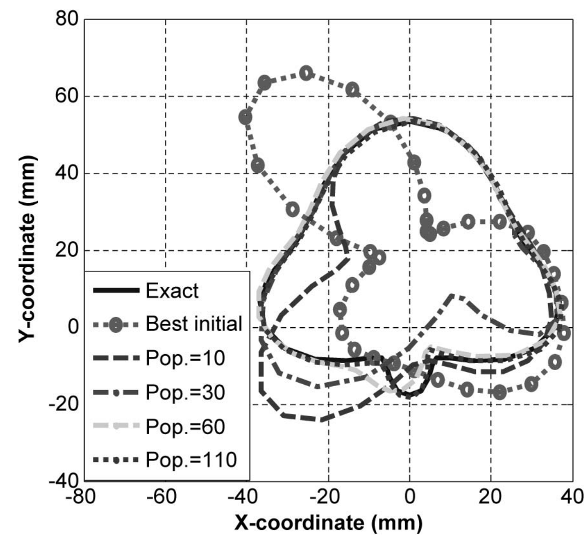

Fig. 15. Exact, reconstructed by SADDE with different population size, and best initial solution. The shape function of this object is given by $F(\theta) = 29.75 + 5.95\cos(4\theta) + 17.85\sin(\theta)$ mm.

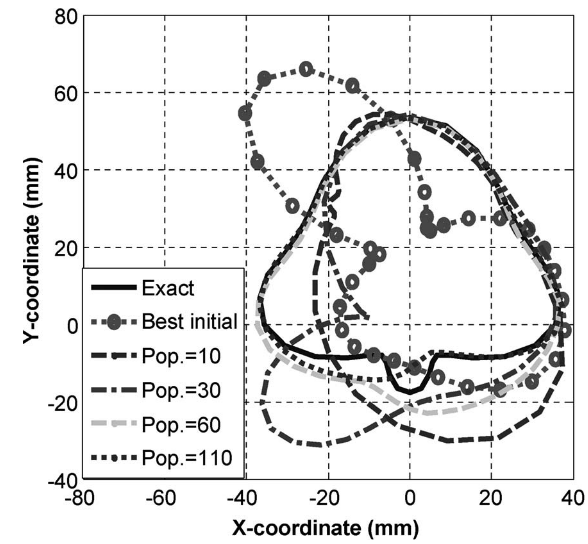

Fig. 17. Exact, reconstructed by DDE with different population size, and best initial solution. The shape function of this object is given by $F(\theta) = 29.75 + 5.95\cos(4\theta) + 17.85\sin(\theta)$ mm.

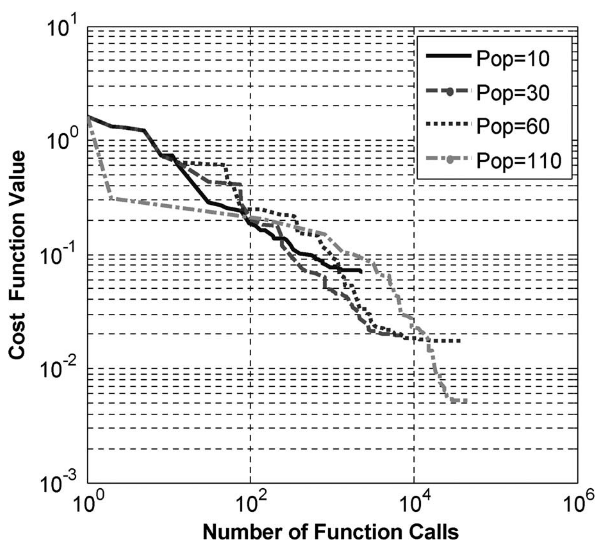

Fig. 16. Cost function (CF) versus numbers of function calls for example 2 by SADDE. The shape function of this object is given by $F(\theta) = 29.75 + 5.95\cos(4\theta) + 17.85\sin(\theta)$ mm.

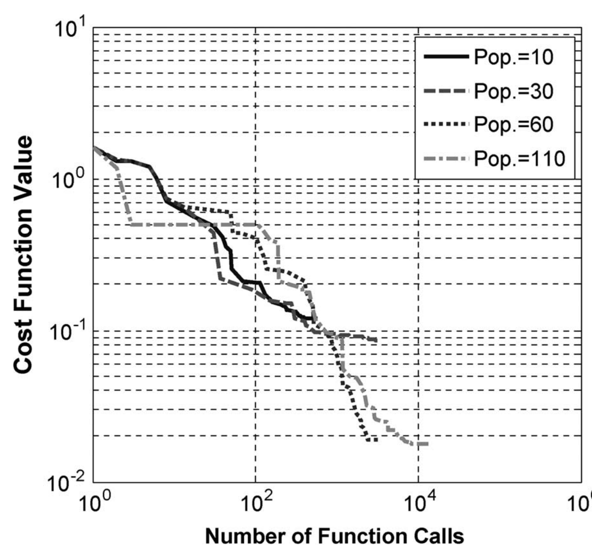

Fig. 18. Cost function (CF) versus numbers of function calls for example 2 by DDE. The shape function of this object is given by $F(\theta) = 29.75 + 5.95\cos(4\theta) + 17.85\sin(\theta)$ mm.

versus generation is shown in Fig. 14. The performance of SADDE is obviously the best for this example.

In the second example, another symmetric but more complex metallic cylinder with shape function $F(\theta) = 29.75 + 5.95\cos(4\theta) + 17.85\sin(\theta)$ mm is considered. Other parameters are kept identical to example 1. The numerical results about the reconstruction and convergence rate of the average CF (after 20 runs) by SADDE, DDE, APSO, and PSO, respectively, are shown in Figs. 15–22. Similarly, these figures show that when the population size is increased the reconstruction quality is improved for all algorithms; in addition, pop $= 110$ is a reasonable choice for the following examples for comparison purpose.

The final reconstructed shapes derived by the four algorithms at the 1000th generation compared to the exact one are plotted in Fig. 23. The relative error of the reconstructed shape $F^{cal}(\theta)$ with respect to the exact one versus generation is shown in Fig. 24. It is shown that in the average sense SADDE is better than PSO, APSO, and DDE in term of searching the global best optima. Moreover, the statistical performances (of 20 runs) of these algorithms applied for examples 1 and 2 with pop $= 110$ are listed in Tables I–IV, respectively. In short, no matter for the CF or the shape function it shows that SADDE outperforms DDE, PSO, and APSO regarding the average sense and the standard deviation.

B. Nonsymmetric of Single-Scatterer Configurations

For the third example, we test a nonsymmetric metallic cylinder with shape function $F(\theta) = 29.75 + 5.95\cos(3\theta) - 5.95\sin(\theta)$ mm, while the other parameters are kept the same as the first example except. The reconstructed image by PSO, APSO, DDE, and SADDE of example 3 for pop $= 110$ is shown in Fig. 25. It is found that the image obtained by

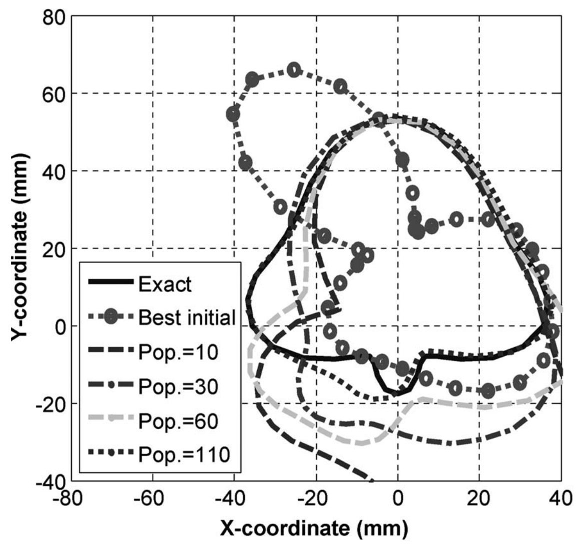

Fig. 19. Exact, reconstructed by APSO with different population size, and best initial solution. The shape function of this object is given by $F(\theta) = 29.75 + 5.95\cos(4\theta) + 17.85\sin(\theta)$ mm.

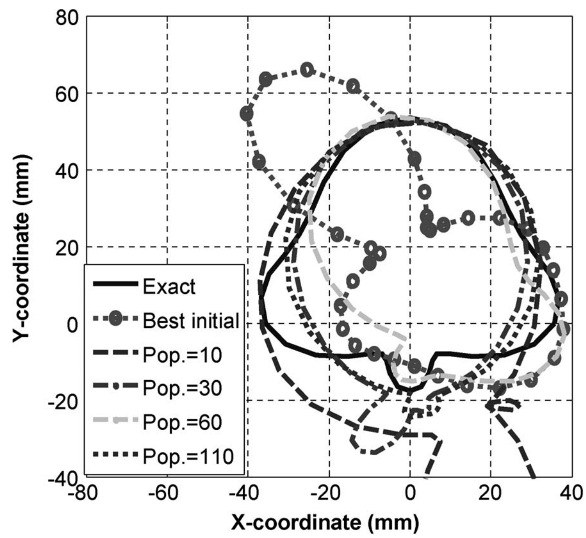

Fig. 21. Exact, reconstructed by PSO with different population size, and best initial solution. The shape function of this object is given by $F(\theta) = 29.75 + 5.95\cos(4\theta) + 17.85\sin(\theta)$ mm.

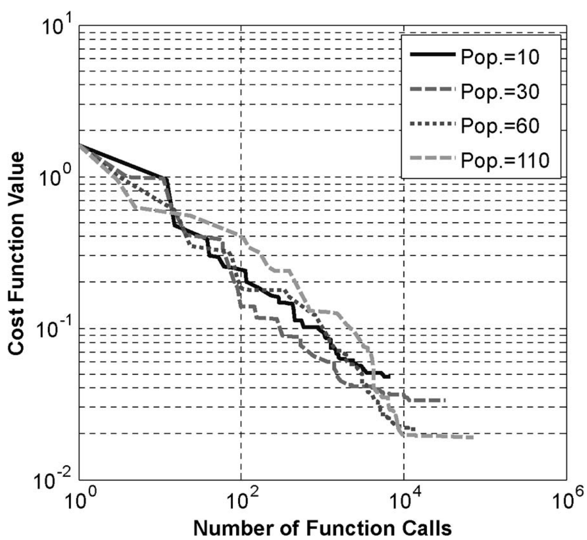

Fig. 20. Cost function (CF) versus numbers of function calls for example 2 by APSO. The shape function of this object is given by $F(\theta) = 29.75 + 5.95\cos(4\theta) + 17.85\sin(\theta)$ mm.

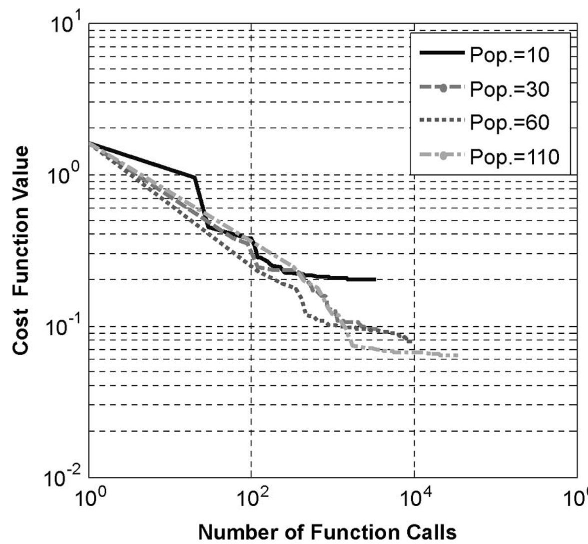

Fig. 22. Cost function (CF) versus numbers of function calls for example 2 by PSO. The shape function of this object is given by $F(\theta) = 29.75 + 5.95\cos(4\theta) + 17.85\sin(\theta)$ mm.

PSO relatively poor as compared with others. Note that the reconstructed shape is the average results (of 20 runs) at the 1000th generation. The CF (CF) versus the number of function calls and the relative error value versus generation are shown in Figs. 26 and 27, respectively. PSO performs relatively poor for this example, while SADDE again outperforms the others in term of the ability of searching the global best optima. Moreover, the statistical performances (of 20 runs) of these algorithms applied for example 3 are listed in Tables V and VI. Again, no matter for the CF or the shape function, it shows that SADDE outperforms DDE, PSO, and APSO regarding the average sense and the standard deviation.

C. Multiple-Scatterers Configurations

In the final example, let us consider the inverse problem with two metallic cylinders. The first metallic cylinder is located at (−61 mm, 57 mm) of which the shape function is $F_1(\theta_1) = 29.75$ mm. The shape function of the second metallic cylinder is $F_2(\theta_2) = 29.75 + 5.95\cos(3\theta_2) + 5.95\sin(\theta_2)$ mm, of which the position is (41 mm, 51 mm). Note that the unknown number is 22 and Pop $= 220$ is set in this case, while other parameters are kept identical to example 1. The reconstructed images at different generations, the CF (CF) versus the number of function calls and relative error value versus generation are shown in Figs. 28–30, respectively. It is found that the final images obtained by these four algorithms are all poor as compared with the exact one. However, it is noted that the locations of the two conductors are correctly identified which is an inherent advantage via the time-domain technique.

Moreover, the statistical performances (of 20 runs) of these algorithms applied for example 4 are listed in Tables VII and VIII. The relative error values by these four algorithms are relatively high (> 0.3) and unacceptable as compared to the

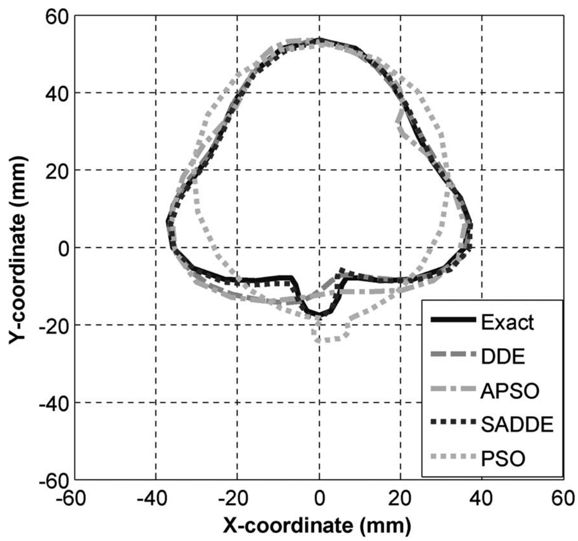

Fig. 23. Reconstructed cross section of the cylinder of example 2 by DDE, APSO, SADDE, and PSO. The shape function of this object is given by $F(\theta) = 29.75 + 5.95\cos(4\theta) + 17.85\sin(\theta)$ mm.

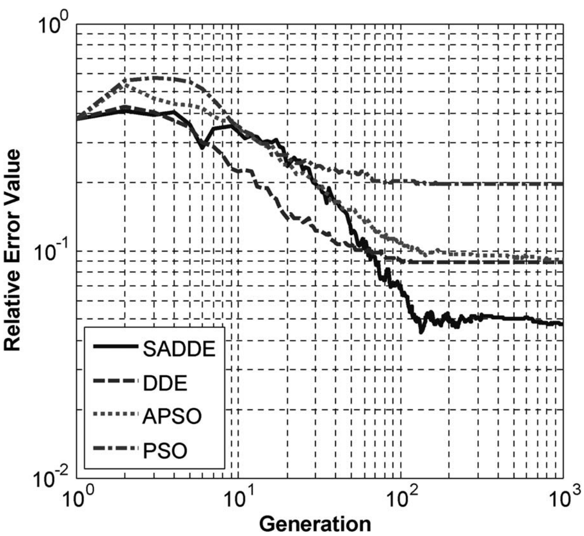

Fig. 24. Shape function error versus generation for example 2 by SADDE, DDE, APSO, and PSO, respectively. The shape function of this object is given by $F(\theta) = 29.75 + 5.95\cos(4\theta) + 17.85\sin(\theta)$ mm.

previous examples. In addition, the standard deviations increase quite a lot for all these four algorithms (> 0.1), which implies that they are unable to effectively and/or efficiently resolve such an inverse problem with two adjacent conductors buried in a layer dielectric medium. Even so, SADDE still outperforms DDE, PSO, and APSO regarding the average sense and the standard deviation. In addition, the best relative error value for shape function achieved by the SADDE is 0.12, which is nearly acceptable. By careful examination of the statistical performances of Tables I–VIII, it should be mentioned the standard deviation for SADDE is small ($\sim$0.01 or less) when it performs well to yield the global the optimum. On the contrary, a large value of standard deviation ($\sim$0.1 or more) for SADDE corresponds to a large relative error for the shape reconstruction. This may lead to a practical rule for shape reconstruction confirmation.

Table IX shows the computational time for the above examples discussed. The extra computational burden is small if

TABLE I
COMPARATIVE RESULTS FOR EXAMPLE 1 (RELATIVE ERROR VALUE)

algorithm	Best	Worst	Mean	St. Dev.
SADDE	0.0138	0.097	0.059	0.028
DDE	0.023	0.253	0.126	0.079
APSO	0.027	0.437	0.171	0.136
PSO	0.057	0.508	0.217	0.105

TABLE II
COMPARATIVE RESULTS FOR EXAMPLE 1 (COST FUNCTION VALUE)

algorithm	Best	Worst	Mean	St. Dev.
SADDE	0.0114	0.035	0.012	0.007
DDE	0.0182	0.055	0.020	0.0145
APSO	0.0188	0.0765	0.036	0.0173
PSO	0.0298	0.1182	0.063	0.0288

TABLE III
COMPARATIVE RESULTS FOR EXAMPLE 2 (RELATIVE ERROR VALUE)

algorithm	Best	Worst	Mean	St. Dev.
SADDE	0.037	0.059	0.047	0.006
DDE	0.039	0.206	0.089	0.049
APSO	0.039	0.198	0.091	0.051
PSO	0.071	0.533	0.196	0.114

TABLE IV
COMPARATIVE RESULTS FOR EXAMPLE 2 (COST FUNCTION VALUE)

algorithm	Best	Worst	Mean	St. Dev.
SADDE	0.0041	0.024	0.005	0.006
DDE	0.0049	0.0538	0.019	0.049
APSO	0.0051	0.0522	0.018	0.051
PSO	0.015	0.108	0.062	0.114

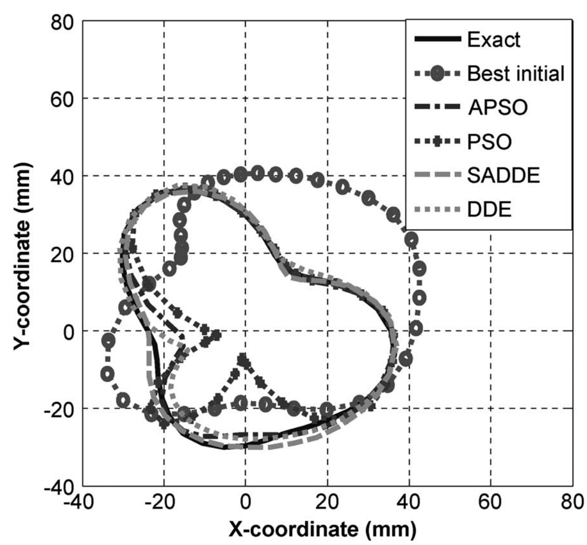

Fig. 25. Reconstructed cross section of the cylinder of example 3 by APSO, PSO, SADDE, and DDE. The shape function of this object is given by $F(\theta) = 29.75 + 5.95\cos(3\theta) - 5.95\sin(\theta)$ mm.

SADDE is employed to achieve better accuracy for the 2-D inverse scattering problems. In fact, the computational burden is roughly the same for SADDE, DDE, and APSO. For the shape reconstruction examples studied, the computation time is dominated by the FDTD procedure for the scattering problems.

D. Noise Analysis

In order to investigate the sensitivity of the imaging algorithm against random noise, the additive white Gaussian noise of zero mean with standard deviation σ_g is added into the

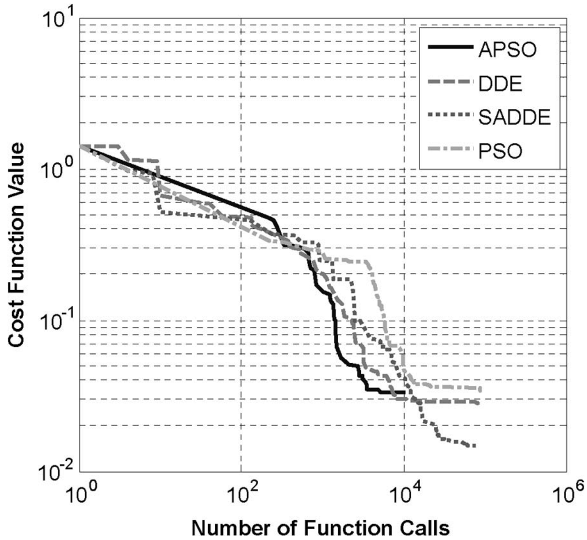

Fig. 26. Value of cost function versus the number of function calls for example 3. The shape function of this object is given by $F(\theta) = 29.75 + 5.95\cos(3\theta) - 5.95\sin(\theta)$ mm.

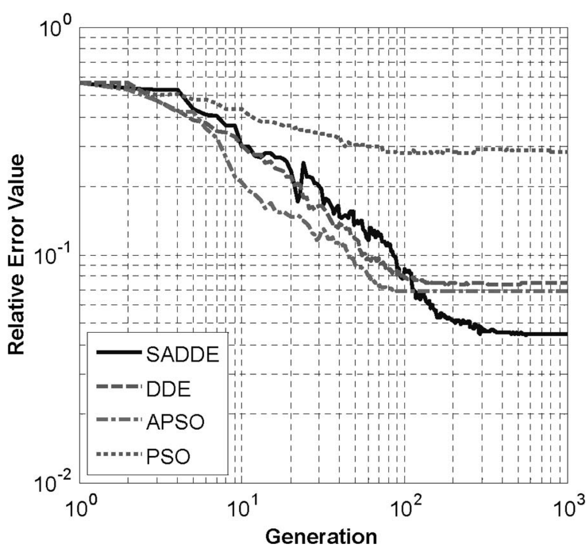

Fig. 27. Shape function error versus generation for example 3 by SADDE, DDE, APSO, and PSO, respectively. The shape function of this object is given by $F(\theta) = 29.75 + 5.95\cos(3\theta) - 5.95\sin(\theta)$ mm.

TABLE V
COMPARATIVE RESULTS FOR EXAMPLE 3 (RELATIVE ERROR VALUE)

algorithm	Best	Worst	Mean	St. Dev.
SADDE	0.040	0.142	0.045	0.011
DDE	0.029	0.114	0.069	0.025
APSO	0.043	0.142	0.075	0.031
PSO	0.054	0.655	0.123	0.201

recorded scattered electric fields to mimic the measurement errors for examples 1 to 3 (example 4 is not included due to its poor quality of shape reconstruction). The signal-to-noise ratio (SNR) is defined as

$$\mathrm{SNR} = 10\log_{10}\frac{\sum_{n=1}^{Ni}\sum_{m=1}^{Mi}\sum_{b=0}^{B}\left|E_z^{\exp}(n,m,b\Delta t)\right|^2}{\sigma_g^2(N_i)(M_i)(B)}. \quad (18)$$

Figs. 31–34 show the reconstructed results for the cylinder under the condition that the recorded scattered fields are contaminated by noise, of which the SNR includes 40 dB, 30 dB, 20 dB, 10 dB, and 3 dB. It is observed that good reconstruction can be obtained for the shape of the metallic cylinder when the SNR is above 10 dB. Moreover, from Figs. 31–34, we conclude that even in case of noisy measurements, SADDE outperforms DDE, PSO, and APSO, in general, and results in more accurate reconstruction.

TABLE VI
COMPARATIVE RESULTS FOR EXAMPLE 3 (COST FUNCTION VALUE)

algorithm	Best	Worst	Mean	St. Dev.
SADDE	0.014	0.033	0.0165	0.002
DDE	0.016	0.044	0.032	0.006
APSO	0.015	0.071	0.0298	0.016
PSO	0.025	0.1495	0.038	0.035

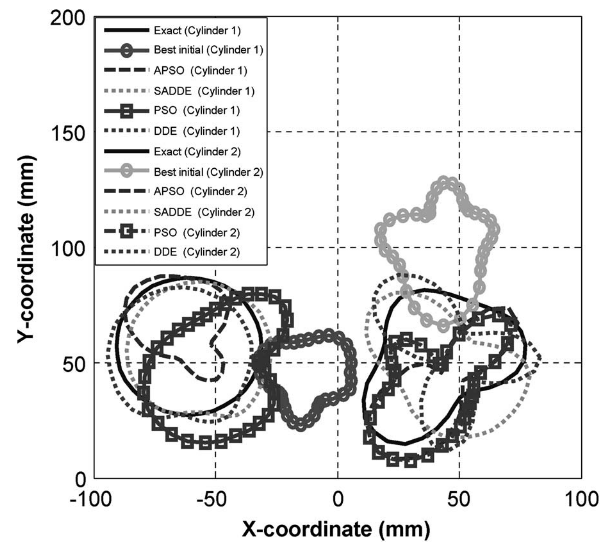

Fig. 28. Reconstructed cross section of the cylinder of example 4 by APSO, PSO, SADDE, and DDE. The shape function of these objects are given by $F_1(\theta_1) = 29.75$ mm and $F_2(\theta_2) = 29.75 + 5.95\cos(3\theta_2) + 5.95\sin(\theta_2)$ mm.

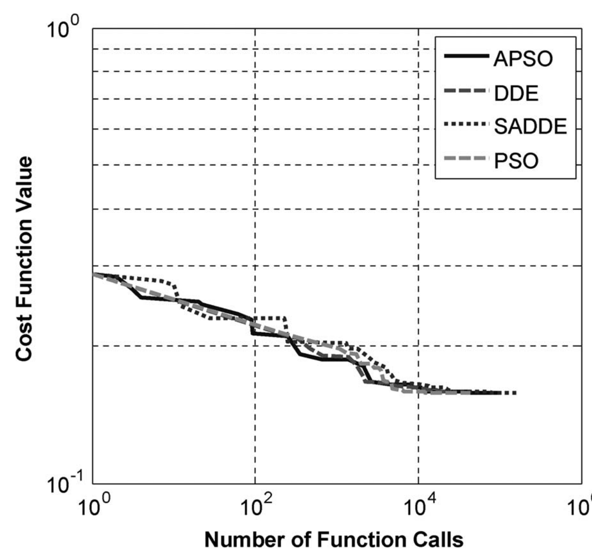

Fig. 29. Value of cost function versus the number of function calls for example 4. The shape function of these objects are given by $F_1(\theta_1) = 29.75$ mm and $F_2(\theta_2) = 29.75 + 5.95\cos(3\theta_2) + 5.95\sin(\theta_2)$ mm.

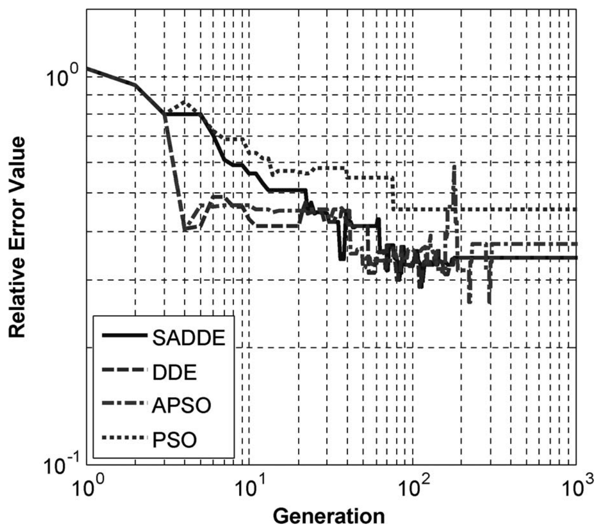

Fig. 30. Shape function error versus generation for example 4 by SADDE, DDE, APSO, and PSO, respectively. The shape function of these objects are given by $F_1(\theta_1) = 29.75$ mm and $F_2(\theta_2) = 29.75 + 5.95\cos(3\theta_2) + 5.95\sin(\theta_2)$ mm.

TABLE VII
COMPARATIVE RESULTS FOR EXAMPLE 4 (RELATIVE ERROR VALUE)

algorithm	Best	Worst	Mean	St. Dev.
SADDE	0.12	0.487	0.341	0.101
DDE	0.258	0.656	0.353	0.180
APSO	0.279	0.782	0.374	0.215
PSO	0.293	1.101	0.458	0.35

TABLE VIII
COMPARATIVE RESULTS FOR EXAMPLE 4 (COST FUNCTION VALUE)

algorithm	Best	Worst	Mean	St. Dev.
SADDE	0.10	0.3	0.171	0.12
DDE	0.120	0.91	0.174	0.21
APSO	0.137	0.98	0.181	0.31
PSO	0.21	1.40	0.187	0.48

TABLE IX
COMPUTATION TIME FOR ALL EXAMPLES (S)

algorithm	Example 1	Example 2	Example 3	Example 4
SADDE	87891	88471	87415	614822
DDE	86873	87439	87116	603571
APSO	83472	84151	87181	605970
PSO	91853	90154	91557	817920

VI. CONCLUSION

In this paper, four population-based optimization algorithms including APSO, PSO, DDE, and SADDE are applied to reconstruct the location and shape of the 2-D metallic cylinder buried in dielectric slab medium. In order to describe the shape of the scatterer more effectively, cubic-spline interpolation technique is utilized.

The statistical performances of these algorithms are reported and shown in Tables I–VIII. For the cases of single conductor, the simulated results show that SADDE outperforms PSO, APSO, and DDE in terms of the ability of exploring the optima. In addition, for either the CF or the shape function concerned, it is concluded that SADDE outperforms DDE, PSO, and APSO regarding the average sense and the standard deviation. However, these results are considered to be indicative

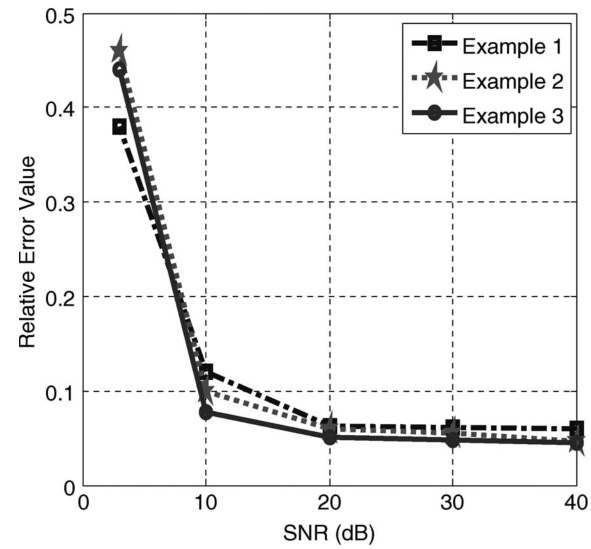

Fig. 31. Shape error as function of SNR(dB) by SADDE.

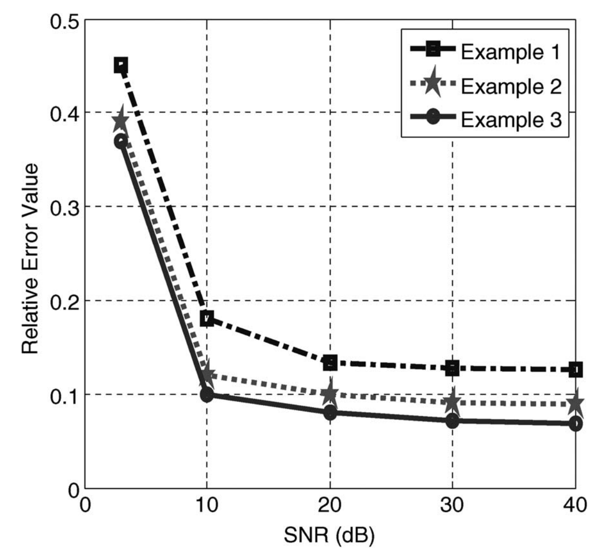

Fig. 32. Shape error as function of SNR(dB) by DDE.

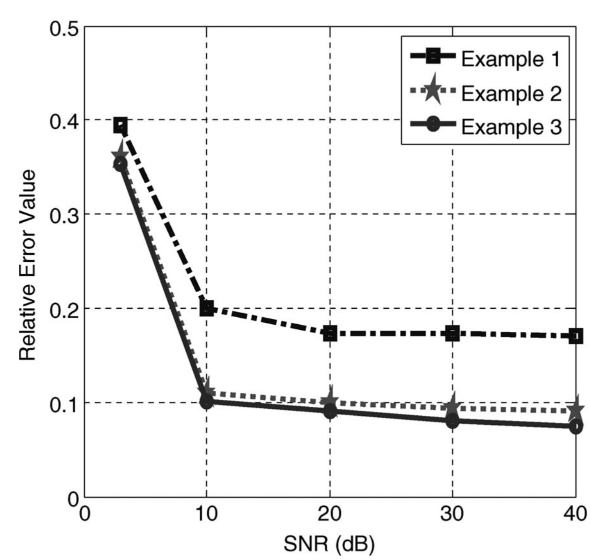

Fig. 33. Shape error as function of SNR(dB) by APSO.

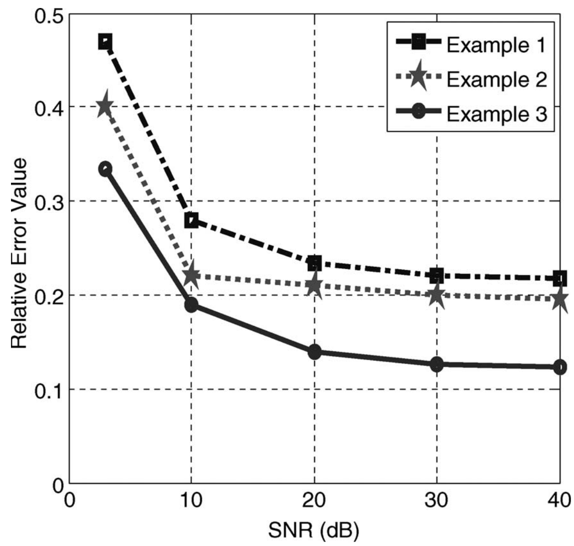

Fig. 34. Shape error as function of SNR(dB) by PSO.

and do not generally apply to all optimization problems in electromagnetics.

The performance of PSO is the worse among the four algorithms compared. In example 3, it is found that the image obtained by PSO is relatively poor as compared with others. The performances of DDE and APSO are comparable, although DDE is a little bit better in general. The possible reasons are due to the implementation of approaching the "Best" and dynamic updating for both algorithms. The outstanding performance of SADDE is due to its ability of self-adaptivity.

In addition, the standard deviations increase quite a lot for all these four algorithms (> 0.1), which implies that they are unable to effectively and/or efficiently resolve such

For the inverse problem with two adjacent conductors buried in a layer dielectric medium, all the four algorithms investigated are unable to effectively and/or efficiently resolve, for which the standard deviations increase quite a lot. However, the best result for shape function achieved by the SADDE is still nearly acceptable, which exhibits the robustness of SADDE.

By careful examination of the statistical performances, it is found that for SADDE the standard deviation (after 20 runs) may be inversely related to relative error for the shape reconstruction. This may lead to a practical rule for shape reconstruction confirmation. The numerical results show that, even in the presence of noisy field measurements, good reconstruction for the shape of the metallic cylinder can be obtained by SADDE when the SNR is above 10 dB. The application of the robust SADDE to other design problems would be made in the future.

REFERENCES

[1] L.-P. Song, C. Yu, and Q. H. Liu, "Through-wall imaging (TWI) by radar: 2-D tomographic results and analyses," *IEEE Trans. Geosci. Remote Sens.*, vol. 43, no. 12, pp. 2793–2798, Dec. 2005.

[2] I. Catapano, L. Crocco, and T. Isernia, "Improved sampling methods for shape reconstruction of 3-D buried targets," *IEEE Trans. Geosci. Remote Sens.*, vol. 46, no. 10, pp. 3265–3273, Oct. 2008.

[3] F. Soldovieri, R. Solimene, and G. Prisco, "A multiarray tomographic approach for through-wall imaging," *IEEE Trans. Geosci. Remote Sens.*, vol. 46, no. 4, pp. 1192–1199, Apr. 2008.

[4] F. Soldovieri, F. Ahmad, and R. Solimene, "Validation of microwave tomographic inverse scattering approach via through-the-wall experiments in semicontrolled conditions," *IEEE Geosci. Remote Sens. Lett.*, vol. 8, no. 1, pp. 123–127, Jan. 2011.

[5] M. Benedetti, D. Lesselier, M. Lambert, and A. Massa, "Multiple-shape reconstruction by means of multiregion level sets," *IEEE Trans. Geosci. Remote Sens.*, vol. 48, no. 5, pp. 2330–2342, May 2010.

[6] K. A. Nabulsi and D. G. Dudley, "A new approximation and a new measurable constraint for slab profile inversion," *IEEE Trans. Geosci. Remote Sens.*, vol. 34, no. 3, pp. 820–823, May 1996.

[7] W. Chien and C. C. Chiu, "Using NU-SSGA to reduce the searching time in inverse problem of a buried metallic object," *IEEE Trans. Antennas Propag.*, vol. 53, no. 10, pp. 3128–3134, Oct. 2005.

[8] X. Chen, "Subspace-based optimization method for solving inverse-scattering problems," *IEEE Trans. Geosci. Remote Sens.*, vol. 48, no. 1, pp. 42–49, Jan. 2010.

[9] G. Franceschini, M. Donelli, R. Azaro, and A. Massa, "Inversion of phaseless total field data using a two-step strategy based on the iterative multiscaling approach," *IEEE Trans. Geosci. Remote Sens.*, vol. 44, no. 12, pp. 3527–3539, Dec. 2006.

[10] P. Mojabi and J. LoVetri, "Overview and classification of some regularization techniques for the gauss-newton inversion method applied to inverse scattering problems," *IEEE Trans. Antennas Propag.*, vol. 57, no. 9, pp. 2658–2665, Sep. 2009.

[11] L. Li, H. Zheng, and F. Li, "Two-dimensional contrast source inversion method with phaseless data: TM case," *IEEE Trans. Geosci. Remote Sens.*, vol. 47, no. 6, pp. 1719–1736, Jun. 2009.

[12] C. Yu, M. Yuan, Y. Zhang, J. Stang, R. T. George, G. A. Ybarra, W. T. Joines, and Q. H. Liu, "Microwave imaging in layered media: 3-D image reconstruction from experimental data," *IEEE Trans. Antennas Propag.*, vol. 58, no. 2, pp. 440–448, Feb. 2010.

[13] F. Li, Q. H. Liu, and L.-P. Song, "Three-dimensional reconstruction of objects buried in layered media using Born and distorted Born iterative methods," *IEEE Geosci. Remote Sens. Lett.*, vol. 1, no. 2, pp. 107–111, Apr. 2004.

[14] P. Rocca, M. Donelli, G. Gragnani, and A. Massa, "Iterative multi-resolution retrieval of non-measurable equivalent currents for the imaging of dielectric objects," *Inv. Probl.*, vol. 25, no. 5, pp. 055004-1–055004-15, May 2009.

[15] I. T. Rekanos, "Time-domain inverse scattering using Lagrange multipliers: An iterative FDTD-based optimization technique," *J. Electromagn. Waves Appl.*, vol. 17, no. 2, pp. 271–289, 2003.

[16] T. Moriyama, Z. Meng, and T. Takenaka, "Forward-backward time-stepping method combined with genetic algorithm applied to breast cancer detection," *Microw. Opt. Technol. Lett.*, vol. 53, no. 2, pp. 438–442, Feb. 2011.

[17] M. Benedetti, D. Lesselier, M. Lambert, and A. Massa, "A multi-resolution technique based on shape optimization for the reconstruction of homogeneous dielectric objects," *Inv. Probl.*, vol. 25, no. 1, pp. 015009-1–015009-26, Jan. 2009.

[18] S. Caorsi, M. Donelli, D. Franceschini, and A. Massa, "A new methodology based on an iterative multiscaling for microwave imaging," *IEEE Trans. Microw. Theory Tech.*, vol. 51, no. 4, pp. 1761–1776, Apr. 2003.

[19] M. Donelli, G. Franceschini, A. Martini, and A. Massa, "An integrated multiscaling strategy based on a particle swarm algorithm for inverse scattering problems," *IEEE Trans. Geosci. Remote Sens.*, vol. 44, no. 2, pp. 298–312, Feb. 2006.

[20] W. Chien, C. H. Huang, C. C. Chiu, and C. L. Li, "Image reconstruction for 2D homogeneous dielectric cylinder using FDTD method and SSGA," *Int. J. Appl. Electromagn. Mech.*, vol. 32, no. 2, pp. 111–123, Feb. 2010.

[21] C. H. Sun, C. L. Liu, K. C. Chen, C. C. Chiu, C. L. Li, and C. C. Tasi, "Electromagnetic transverse electric wave inverse scattering of a partially immersed conductor by steady-state genetic algorithm," *Electromagnetics*, vol. 28, no. 6, pp. 389–400, Aug. 2008.

[22] M. Pastorino, "Stochastic optimization methods applied to microwave imaging: A review," *IEEE Trans. Antennas Propag.*, vol. 55, no. 3, pp. 538–548, Mar. 2007.

[23] P. Rocca, M. Benedetti, M. Donelli, D. Franceschini, and A. Massa, "Evolutionary optimization as applied to inverse scattering problems," *Inv. Probl.*, vol. 25, no. 12, pp. 123003-1–123003-44, Dec. 2009.

[24] M. Benedetti, R. Azaro, and A. Massa, "Memory enhanced PSO-based optimization approach for smart antennas control in complex interference scenarios," *IEEE Trans. Antennas Propag.*, vol. 56, no. 7, pp. 1939–1947, Jul. 2008.

[25] L. Lizzi, F. Viani, R. Azaro, and A. Massa, "A PSO-driven spline-based shaping approach for ultra-wideband antenna synthesis," *IEEE Trans. Antennas Propag.*, vol. 56, no. 8, pp. 2613–2621, Aug. 2008.

[26] L. Poli, P. Rocca, L. Manica, and A. Massa, “Handling sideband radiations in time-modulated arrays through particle swarm optimization,” *IEEE Trans. Antennas Propag.*, vol. 58, no. 4, pp. 1408–1411, Apr. 2010.
[27] A. Semnani and M. Kamyab, “An enhanced method for inverse scattering problems using Fourier series expansion in conjunction with FDTD and PSO,” *Progr. Electromagn. Res. (PIER)*, vol. 76, pp. 45–64, 2007.
[28] A. Semnani and M. Kamyab, “An enhanced hybrid method for solving inverse scattering problems,” *IEEE Trans. Magn.*, vol. 45, no. 3, pp. 1534–1537, Mar. 2009.
[29] I. T. Rekanos and A. Trochidis, “Shape reconstruction of two-dimensional acoustic obstacle using particle swarm optimization,” *Acta Acust. United With Acustica*, vol. 93, no. 6, pp. 917–923, Nov./Dec. 2007.
[30] C. C. Chiu, C. H. Sun, and W. L. Chang, “and asynchronous particle swarm optimization for inverse scattering of a two-dimensional perfectly conducting cylinder,” *Int. J. Appl. Electromagn. Mech.*, vol. 35, no. 4, pp. 249–261, Apr. 2011.
[31] A. Semnani, M. Kamyab, and I. T. Rekanos, “Reconstruction of one-dimensional dielectric scatterers using differential evolution and particle swarm optimization,” *IEEE Geosci. Remote Sens. Lett.*, vol. 6, no. 4, pp. 671–675, Oct. 2009.
[32] M. Donelli and A. Massa, “Computational approach based on a particle swarm optimizer for microwave imaging of two-dimensional dielectric scatterers,” *IEEE Trans. Microw. Theory Tech.*, vol. 53, no. 5, pp. 1761–1776, May 2005.
[33] I. T. Rekanos, “Shape reconstruction of a perfectly conducting scatterer using differential evolution and particle swarm optimization,” *IEEE Trans. Geosci. Remote Sens.*, vol. 46, no. 7, pp. 1967–1974, Jul. 2008.
[34] A. Semnani, I. T. Rekanos, M. Kamyab, and T. G. Papadopoulos, “Two-dimensional microwave imaging based on hybrid scatterer representation and differential evolution,” *IEEE Trans. Antennas Propag.*, vol. 58, no. 10, pp. 3289–3298, Oct. 2010.
[35] P. Rocca, G. Oliveri, and A. Massa, “Differential evolution as applied to electromagnetics,” *IEEE Antennas Propag. Mag.*, vol. 53, no. 1, pp. 38–49, Feb. 2011.
[36] A. Qing, “Dynamic differential evolution strategy and applications in electromagnetic inverse scattering problems,” *IEEE Trans. Geosci. Remote Sens.*, vol. 44, no. 1, pp. 116–125, Jan. 2006.
[37] C. H. Sun, C. C. Chiu, C. L. Li, and C. H. Huang, “Time domain image reconstruction for homogenous dielectric objects by dynamic differential evolution,” *Electromagnetics*, vol. 30, no. 4, pp. 309–323, May 2010.
[38] J. Brest, S. Greiner, B. Boskovic, M. Mernik, and V. Zumer, “Self-adapting control parameters in differential evolution: Comparative study on numerical benchmark problems,” *IEEE Trans. Evol. Comput.*, vol. 10, no. 6, pp. 646–657, Dec. 2006.
[39] S. K. Goudos, K. Siakavara, T. Samaras, E. E. Vafiadis, and J. N. Sahalos, “Self-adaptive differential evolution applied to real-valued antenna and microwave design problems,” *IEEE Trans. Antennas Propag.*, vol. 59, no. 4, pp. 1286–1298, Apr. 2011.
[40] M. W. Chevalier, R. J. Luebbers, and V. P. Cable, “FDTD local grid with material traverse,” *IEEE Trans. Antennas Propag.*, vol. 45, no. 3, pp. 411–421, Mar. 1997.
[41] C. de Boor, *A Practical Guide to Splines*. New York: Springer-Verlag, 1978.
[42] K. Yee, “Numerical solutions of initial boundary value problems involving Maxwell’s equations in isotropic media,” *IEEE Trans. Antennas Propag.*, vol. AP-14, no. 3, pp. 302–307, May 1966.
[43] C. L. Li, C. W. Liu, and S. H. Chen, “Optimization of a PML Absorber’s conductivity profile using FDTD,” *Microw. Opt. Technol. Lett.*, vol. 37, no. 5, pp. 380–383, 2003.
[44] R. Storn and K. Price, “Differential evolution—A simple and efficient adaptive scheme for global optimization over continuous spaces,” Int. Comput. Sci. Inst., Berkeley, CA, Tech. Rep. TR-95-012, 1995.
[45] J. Kennedy and R. C. Eberhart, “Particle swarm optimization,” in *Proc. IEEE Int. Conf. Neural Netw.*, 1995, pp. 1942–1948.
[46] M. Clerc, “The swarm and the queen: Towards a deterministic and adaptive particle swarm optimization,” in *Proc. Congr. Evol. Comput.*, Washington, DC, 1999, pp. 1951–1957.
[47] T. Huang and A. S. Mohan, “A hybrid boundary condition for robust particle swarm optimization,” *IEEE Antennas Wireless Propag. Lett.*, vol. 4, pp. 112–117, 2005.
[48] W. Chien and C. C. Chiu, “Cubic-Spline expansion with GA for a partially immersed conducting cylinder,” *IEICE Trans. Electron*, vol. E88-C, no. 12, pp. 2223–2228, Dec. 2005.
[49] A. Carlisle and G. Dozier, “An off-the-shelf PSO,” in *Proc. Workshop Particle Swarm Optim.*, 2001, pp. 1–6.

Chien-Ching Chiu received the B.S.C.E. degree from National Chiao Tung University, Hsinchu, Taiwan, in 1985, and the M.S.E.E. and Ph.D. degrees from National Taiwan University, Taipei, Taiwan, in 1987 and 1991, respectively.

From 1987 to 1989, he was a Communication Officer with the ROC Army Force. In 1992, he joined the faculty of the Department of Electrical Engineering, Tamkang University, New Taipei City, Taiwan, where he is now a Professor. From 1998 to 1999, he was a Visiting Scholar at the Massachusetts Institute of Technology, Cambridge, and the University of Illinois at Urbana-Champaign, Urbana. He is a Visiting Professor with the University of Wollongong, Wollongong, Australia, in 2006. Moreover, he was a Visiting Professor with the University of London, London, U.K., in 2011. His current research interests include microwave imaging, numerical techniques in electromagnetics, indoor wireless communications, and ultrawideband communication systems. He has published more than 100 journal papers on inverse scattering problems, communication systems, and optimization algorithms.

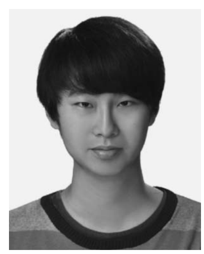

Chi-Hsien Sun received M.S.E.E. and Ph.D. degrees in electrical engineering from Tamkang University, Taipei, Taiwan, in 2008 and 2012, respectively.

His special interests include theoretical and computational electromagnetics, and application of various optimization schemes such as the steady-state genetic algorithm, particle swarm optimization, dynamic differential evolution (DDE), self-adaptive DDE, and the Taguchi method in electromagnetics.

Ching-Lieh Li was born November 24, 1963, in Pingtun, Taiwan. He received the B.S. degree from National Taiwan University, Taipei, Taiwan, in 1985, and the M.S. and Ph.D. degrees from Michigan State University, East Lansing, in 1990 and 1993, respectively, all in electrical engineering.

From 1989 to 1993, he was a Research Assistant in the Electrical Engineering Department, Michigan State University, where he worked on the measurement techniques for determining the electromagnetic properties of materials. In 1993, he joined the Electrical Engineering Faculty at Tamkang University, Taipei, where now he is a Professor. Currently, his research activities involve inverse scattering problem, and microstrip antenna design and dielectric material characterization, etc. His areas of special interest include theoretical and computational electromagnetics, and application of various optimization schemes such as steady-state genetic algorithm, particle swarm optimization, differential evolution, and Taguchi method to electromagnetics.

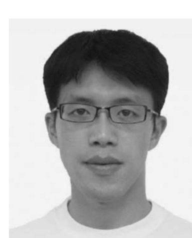

Chung-Hsin Huang was born in New Taipei City, Taiwan, Republic of China, on February 1, 1980. He received the M.S.E.E. and Ph.D. degrees in electrical engineering from Tamkang University, Taipei, Taiwan, in 2004 and 2009, respectively.

Currently, he is an Assistant Professor with the Department of Computer and Communication Engineering, Taipei College of Maritime Technology, Taipei. His current research interests include electromagnetic wave theory and applications, optimization methods, dielectric material characterization, and wireless communications.